Tecnical University of Munich
Department of Physics
Experimental Physics with Cosmic Particles

Bachelor Thesis in Physics

Muon Tracker for the Second Pathfinder of the Pacific Ocean Neutrino Explorer

Eva Laura Winter

5$^{\text{th}}$ of July, 2019

Matriculation No.: 03673381
First Examiner: Prof. Dr. Elisa Resconi
Second Examiner: Prof. Dr. Bastian Märkisch

Abstract

This Bachelor thesis reports on the development of a devise to track muons. As part of STRAW-b (*STRings for Absorption length in Water part b*), it will be deployed in the North Pacific several hundred miles away from Vancouver Island in Canada.

After a feasibility study of the expected muon flux, energy loss in scintillators, coincidental events and reconstruction of the incident angle of the muon, calculations of the light detection efficiency with silicon photomultiplier (SiPM) arrays will be presented. The design of the final muon tracker module is based on those studies and the given parameters by the glass sphere it will be deployed in. How the design is further influenced by measurements of the reflectivity and the transmission of teflon samples and reflective foil will be explained in this thesis.

The main focus will be on the characterisation measurements of the SiPM arrays when illuminated with the same light pulse. The linear increase of the gain with increasing supply voltage and decreasing temperature will be derived, experimentally. Eventually, the proof of concept will be given with first results of the muon detection in the laboratory.

Contents

Introduction

Multi-messenger astronomy uses messenger particles of the four known nature's fundamental forces to analyse astrophysical objects. Its main goal is to understand the processes within those objects that lead to the emission of high-energy particles. The development of a new large-scale neutrino telescope benefits from recent progresses in neutrino astronomy.

In 2018, with the help of *Ocean Network Canada* (ONC), a first pathfinder for such a neutrino telescope was deployed in the Cascadia Basin, an abyssal plain in the North Pacific several hundred miles away from Vancouver Island in Canada, at a depth of about 2660 m. The *STRings for Absorption length in Water* (STRAW) compromise two 120 m long mooring lines instrumented with *Precision Optical Calibration Modules* (POCAM) and *STRAW Digital Optical Modules* (sDOM). The main goals of STRAW are the measurement of light extinction and bioluminescence [1, 10].

As a complement to those measurements, STRAW-b was developed over the last months. This 450 m long mooring line will host glass spheres with standard and specialised modules, one of which will be a muon tracker. Before giving a short overview of the STRAW-b concept and presenting the development of the muon tracker, the theoretical background will be outlined in the following.

Chapter 1

Theoretical Background

This chapter helps to understand what the elementary particles of interest in this experiment, atmospheric muons, are and where they originate from.

1.1 Elementary Particles in the Standard Model

The Standard Model describes all known elementary particles and their interactions. A summarising illustration is given in figure 1.1.

The following gives a short overview of the three families of fermions and their connection with the strong, electromagnetic and weak interactions as well as the exchange particles, also called *mediators*.

1.1.1 Fermions

The fundamental particles of the Standard Model are *quarks* and *leptons*. They have half-integer spin and are therefore *fermions*. In ascending order of their masses they are divided into three families with different flavour quantum numbers. Whereas quarks carry colour and electric charge, charged leptons only have the latter. Neutrinos do not have electric charge. Further, fermions have antiparticles with the same mass but opposite electric charge. A summary of the fundamental fermions (without anti-fermions), their classification into the families and their electric charge is given in table 1.1 [7, 19].

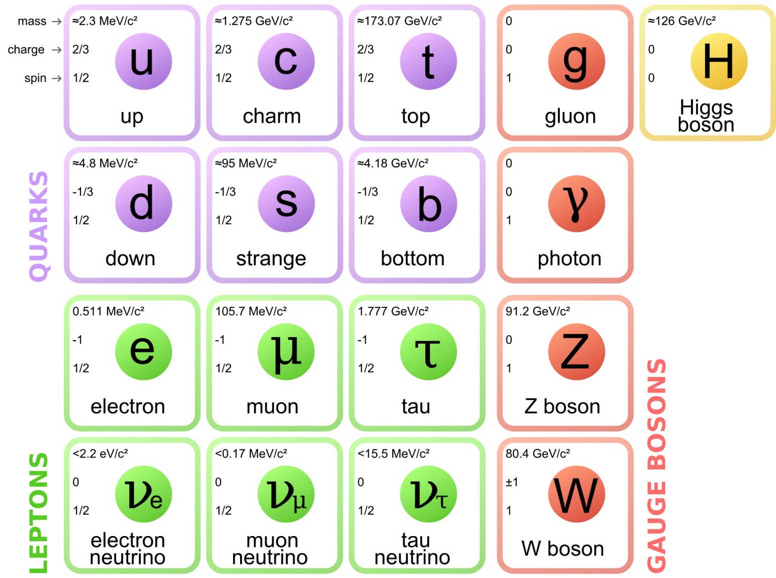

Figure 1.1: *Illustration of the Standard Model of particle physics. Displayed are the elementary particles: quarks (purple) and leptons (green) as well as the mediators of the fundamental interactions: gauge bosons (red) and the Higgs boson (yellow). Figure taken from [20].*

Fermions	**Families**			**Electric Charge**
	1	2	3	[e]
quarks	u	c	t	+2/3
	d	s	b	-1/3
leptons	ν_e	ν_μ	ν_τ	0
	e	μ	τ	-1

Table 1.1: *Summary of the fermions of the Standard Model: quarks and leptons. Classified into the three families and values of their electric charge [19, p. 205].*

1.1.2 Bosons

The exchange particles of the interactions are called *bosons*. The mediators of the interaction between quarks, the *strong* interaction, are the *gluons* (g). They carry colour and have no mass. Another massless particle is the *photon* (γ), the mediator of the *electromagnetic* interaction, which has therefore an infinite effective range. It couples to electric charge. The exchange particles of the *weak* interaction are the massive $W^\pm$ and Z^0 bosons which couple to flavour charge. The gravitational interaction is not included in the Standard Model. Table 1.2 summarises the discussed characteristics of the three interactions [7, 19].

Interaction	**Mediator**	**Mass** [GeV/c^2]	**Coupling**	**Affected fermions**
strong	g	0	colour	q
electromagn.	γ	0	charge	q, e, μ, τ
weak	$W^{\pm}$, Z^0	~ 10^2	flavour	q, e, μ, τ, ν

Table 1.2: *Summary of the three interactions in the Standard Model. Corresponding mediators, their masses, coupling and affected fermions [19, p. 205f].*

1.2 Hadrons

According to today's state of knowledge, regular matter consists of these known elementary particles of the Standard Model. *Hadrons* are held together by the strong interaction between quarks and are divided into two classes: *mesons* and *baryons*. The former are produced in collisions of high-energy particles and are mostly unstable. They consist of one quark and one anti-quark and have therefore integer spin. The lightest mesons are pions, which decay into the even lighter leptons or photons. There are three quark-anti-quark-pairs for the three different pions: [3, 19]

$$|\pi^+\rangle = |\mathrm{u\bar{d}}\rangle \qquad |\pi^-\rangle = |\mathrm{\bar{u}d} \qquad |\pi^0\rangle = \frac{1}{\sqrt{2}}\,|\mathrm{u\bar{u}} - \mathrm{d\bar{d}}\rangle$$

The charged π-mesons decay through weak interaction with a mean lifetime of $2.6 \cdot 10^{-18}$ s in the equally charged muons and neutrinos. The neutral pion decays through electromagnetic interaction into two photons [3, 28]. The π^+-decay is graphically displayed with a Feynman-diagram in figure 1.2.

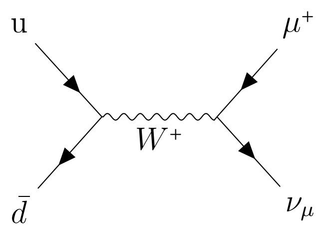

Figure 1.2: *Feynman-diagram of the π^+-decay. Shown is the weak interaction between u- and $\bar{d}$-quark with μ^+ and ν_μ. Mediator of this interaction is the W^+-boson.*

The other class of hadrons are baryons which contain of three quarks or three anti-quarks and have half-integer spin. The lightest baryons are the proton (uud) and the neutron (udd) [19].

1.3 Cosmic Particles

Cosmic rays consist of particles such as protons, α-particles and also heavier elements with extraterrestrial or even extragalactic origin. There is a difference between primary and secondary radiation of which the former are particles that reach Earth undisturbed. Whereas, due to interactions between each other or with particles in the Earth's atmosphere, secondary particles can be created in spallation reactions and particle decays [8].

1.3.1 Primary and Secondary Rays

The primary radiation contains mainly of protons, some α-particles and a few elements with $Z \geq 3$. Protons and α-particles originate mostly from the sun which continuously emits mass through solar winds. High-energy particles, with up to $10^{20}\,\mathrm{eV}$, are believed to have their origin in other galactic or extragalactic objects. The enormous energy release at a supernova explosion is found to be one of the main origins of cosmic rays. Further, rays with non-stellar origin are thought to emerge form active galactic nuclei (AGNs) or blazars. Those incident particles can be detected if either measured before their interaction with nuclei in the Earth's atmosphere starting at an altitude of about 40 km or through shower [8].

Secondary particles are generated by primaries interacting with air nuclei. When hitting such an atmospheric nucleus, charged particles often create unstable hadrons, such as pions or kaons, which then decay into lighter particles [8]. Resulting muons are either then detected on Earth or decay before that in electrons and neutrinos. Like this, a proton with e.g. $10^{15}\,\mathrm{eV}$ can produce more than one million secondaries [3].

Below, the reaction equations of the deep inelastic scattering between a proton (p) and an atmospheric nucleus (N) and of the pion decays are given.

$$\mathrm{p} + \mathrm{N} \rightarrow n_1 \cdot \mathrm{p} + n_2 \cdot \mathrm{n} + n_3 \cdot \pi + n_4 \cdot \mu$$

(with n_i an energy–dependant number)

$$\pi^+ \rightarrow \mu^+ + \nu_\mu$$
$$\mu^+ \rightarrow \mathrm{e}^+ + \nu_\mathrm{e} + \bar{\nu}_\mu$$

$$\pi^- \rightarrow \mu^- + \bar{\nu}_\mu$$
$$\mu^- \rightarrow \mathrm{e}^- + \nu_\mu + \bar{\nu}_\mathrm{e}$$

$$\pi^0 \rightarrow \gamma\gamma$$

Thus, these so-called air showers have a hadronic component developing in an electromagnetic component (photons, electrons and positrons) and a penetrating component consisting of muons and neutrinos [25]. In figure 1.3, a simplified sketch of a cascade shows how the generated elementary particles reach the Earth's surface.

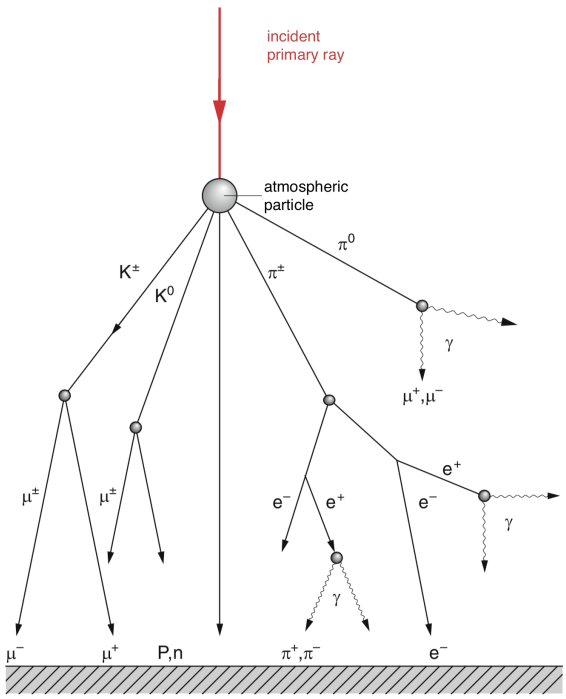

Figure 1.3: *The image shows a cascade formation generated by a cosmic particle interacting with an atmospheric nucleus. The produced unstable hadrons then decay into elementary particles. The created photons, electrons, positrons, muons and neutrinos can be detected on Earth. Figure taken from [3, p. 258] and modified.*

1.3.2 Atmospheric Muons

Measured at sea level approximately 80% of the charged secondary particles are muons. This means a muon flux of about 1 particle per cm^2 per minute through a horizontal area [8].

To understand how muons, with a lifetime $\tau_\mu = 2.2\,\mu$s, can actually reach Earth, special relativity has to be taken into account. As the primary particles have energies between GeV and 10^{20} eV [6] high-energy secondaries are created also. Typically, pions are produced at an altitude of 15 km and then decay, depending on their energy, after a relatively short distance in the range of metres to kilometres. At low energies the resulting muons decay already in the atmosphere and do not reach the detectors on the ground. At very high energies those pions interact to tertiary pions, which only then decay into lower energy muons. Those discrepancies in the momentum-spectra can be seen in figure 1.4 [8].

Figure 1.4: *The image shows the muon-spectrum at Sea level in comparison to the parent-spectrum of the produced pions. The spectra are fairly consistent for momenta between 10 and 100 GeV. At energies < 10 GeV and > 100 GeV the muon intensity is reduced in comparison to the pions. Figure taken from [8, p. 209].*

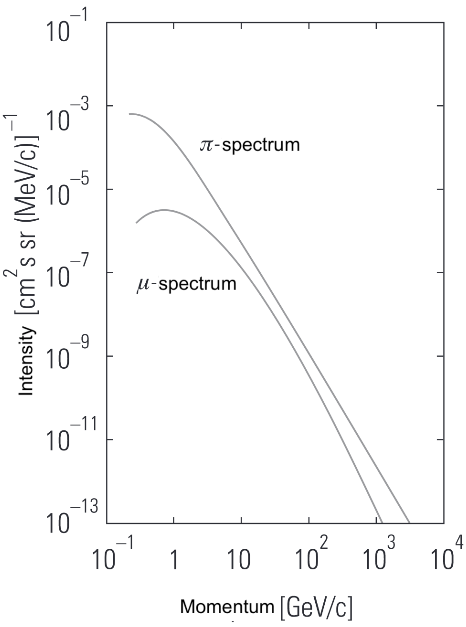

The detected muon-spectrum shows events at energies in the range of $10^{-1} - 10^3$ GeV. A muon with an energy of 1 GeV has a gamma-factor of $\gamma = E/m_\mu c^2 = 9,4$ ($m_\mu = 105.65837$ MeV [28]) and, therefore, a mean path length of $s_\mu \approx \gamma\tau_\mu c = 6.2$ km. That explains why most of the muons reaching the ground are relativistic [8].

Furthermore, the detected intensity of the muon flux is angular-dependent and can be calculated by formular 1.1 where θ is the zenith angle. The angular dependency varies with the muon energy. Above a certain energy is this variation negligible. Here, the exponent of the cosine is $n = 2$ [8].

$$I_\mu(\theta) = I_\mu(\theta = 0) \cdot \cos^n(\theta) \tag{1.1}$$

The intensity of muons coming perpendicularly towards Earth is described at $\theta = 0°$. This does not apply for big zenith angles, because of the lower mass distribution at inclined incident directions. In this case the pions interact less with atmospheric nuclei and more high-energy muons are produced by decays [8].

1.4 Passage of Particles Through Matter

The detection of cosmic particles on Earth is based on their interaction with detector matter. In section 1.1.2, the different interactions for elementary particles were already discussed. For the description of radiation passing through matter, it is in the following differentiated between charged and neutral particles.

Photons can deposit their energy E_γ when passing a medium in three different ways. Firstly, the *photoelectric absorption* where a photon transfers its energy to an atomic electron and the following ejection of the electron from the atom. This outgoing electron has the energy of the incident photon minus the binding energy of the electron. The atom absorbs the recoil momentum. Another interaction of photons with matter is *Compton scattering* on essentially free electrons. After this inelastic impact, the photon travels with a larger wavelength and the electron recoils. The third effect is *pair production*, where a photon with $E_\gamma > 2m_ec^2$ produces an e^+e^--pair in the Coulomb-field of the atom. The nucleus recoils due to energy and momentum conservation. The other uncharged particles are neutrons which transfer energy via elastic scattering with the nuclei [3, 16].

More important for this thesis are the interactions of *charged* particles with matter. Two characteristics can be observed: energy loss and a deviation of the particle's incident direction. Those effects mainly emerge from inelastic collisions with shell electrons where a particle transfers some of its energy through electromagnetic interaction. This causes excitation or even ionisation. The amount of transferred energy is dependent on the energy of the incident particle. It is usually a small fraction of its kinetic energy. As seen in figure 1.4, atmospheric muons detected at sea level have mainly energies from 1 to 100 GeV. Not as often, but also important, is the energy loss due to elastic scattering with nuclei of matter. Although, the amount of transferred energy is usually not as high because of the greater mass of the nuclei of most materials [16].

By far not as frequent as these processes are the deflection of a charged particle in the atomic Coulomb-field. This deflection results in deceleration and therefore, in the emission of photons. This effect is called *Bremsstrahlung* and occurs mainly for electrons or positrons. Another interaction with electromagnetic radiation is the emission of *Cherenkov light*, when a charged particle passes a medium at a velocity greater than the speed of light in this medium. The charged particle causes short-term polarisation of an atom's electron shell. This results in a time-varying electric dipole moment which emits electromagnetic radiation [3, 16].

As those processes are mass-dependent, except of Cherenkov radiation, it makes sense to divide the charged particles in two classes: light particles (electrons and positrons) and heavy ones (muons, pions, α-particles, and light nuclei) [3, 16].

Bethe-Bloch-Formula While travelling a distance $\tilde{x}$ through a medium, charged particles loose energy due to excitation or ionisation processes. The stopping power $-\mathrm{d}E/\mathrm{d}\tilde{x}$ [MeV cm^{-1}] of heavy, charged particles ($m \gg m_e$) is described by the *Bethe-Bloch-formula* (1.2) [16, 28].

$$-\frac{\mathrm{d}E}{\mathrm{d}\tilde{x}} = 2\pi N_A r_e^2 m_e c^2 \rho \frac{Z}{A}\frac{z^2}{\beta^2}\left[\ln\left(\frac{2m_e\gamma^2 v^2 W_{max}}{I^2}\right) - 2\beta^2\right] \tag{1.2}$$

With the natural constants:

$$\begin{aligned} N_A &= 6.022 \cdot 10^{23}\,/\mathrm{mol}, \text{ Avogadro's number} \\ r_e &= 2.817 \cdot 10^{-13}\,\mathrm{m}, \text{ electron radius} \\ m_e &= 510.9989\,\mathrm{keV/c^2}, \text{ electron mass} \\ c &= 2.998 \cdot 10^{8}\,\mathrm{m/s}, \text{ speed of light} \end{aligned}$$

characteristics of the charged particle (with mass M):

$$
\begin{aligned}
z &: \text{ electric charge in units of } e \\
\beta &= \frac{v}{c}, \text{ velocity in units of } c \\
\gamma &= \frac{1}{\sqrt{1-\beta^2}}, \text{ relativistic gamma-factor} \\
W_{max} &= \frac{2m_e c^2 \beta^2 \gamma^2}{1 + 2\gamma m_e/M + (m_e/M)^2}, \text{ maximum energy transfer in a single collision}
\end{aligned}
\tag{1.3}
$$

and characteristics of the material:

$$
\begin{aligned}
\rho &: \text{ density} \\
Z &: \text{ atomic number} \\
A &: \text{ atomic weight} \\
I &= 16\,\mathrm{eV} \cdot Z^{0.9}, \text{ mean excitation potential [19]}
\end{aligned}
\tag{1.4}
$$

The magnitude of the energy loss is dependent on the medium as it is proportional to the term $\rho N_A Z/A$, which describes the electron density n_e of the medium. For most of the atoms applies $Z/A \approx 0.5$ and with N_A being constant, for comparison $-\mathrm{d}E/\mathrm{d}\tilde{x}$ is divided by the density ρ and $x \equiv \rho\tilde{x}$ is defined as the density times the travelled distance in g/cm^2 [17]. Figure 1.5 shows the behaviour of $\langle -\mathrm{d}E/\mathrm{d}x\rangle$ [MeV g^{-1} cm^2] depending on the corresponding particle momentum for muons, pions and protons in different materials.

The rapid falling for smaller values of $\beta\gamma$, and therefore increasing velocity of the particle, originates from the $1/\beta^2$-factor in equation 1.2. At values in the range of 3 to 4 for $\beta\gamma$ the curves show a minimum, where the least ionisation happens. At higher values, the curve is dominated by the logarithmic term and reflects a *relativistic rise* of the energy loss [17].

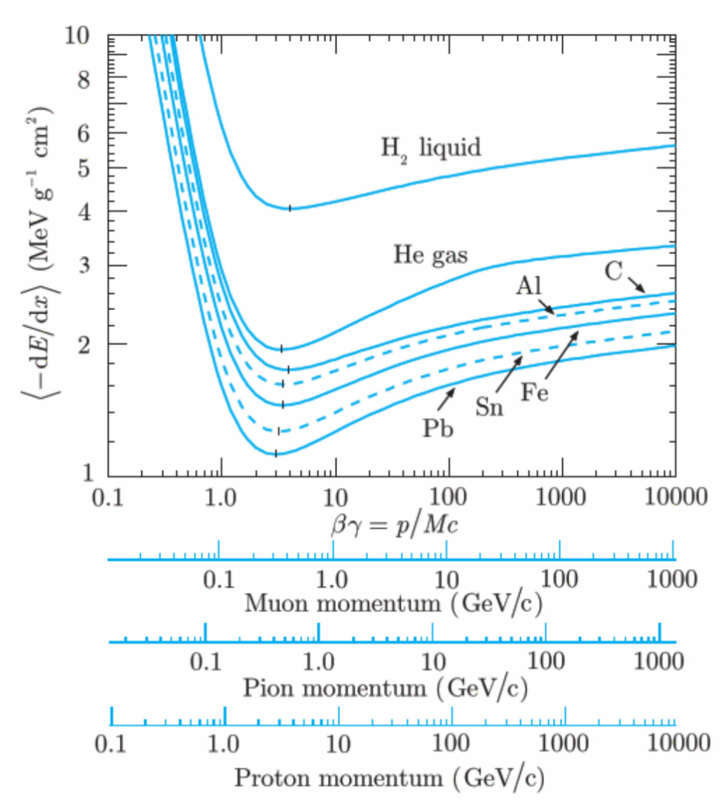

Figure 1.5: *Energy loss according to Bethe-Bloch-formula for muons, pions and protons in different materials. Another x-axis shows the dependency on $\beta\gamma = p/Mc$. $-\mathrm{d}E/\mathrm{d}x$ is given in [MeV g^{-1} cm^2] as $x = \tilde{x} \cdot \rho$ [g/cm^2] is the density multiplied by the distance. Figure taken from [17, p. 90].*

Chapter 2

Experimental Methods

The detection of charged particles is possible due to their interaction with matter. It is taken advantage of the resulting optical (fluorescence) and electrical (ionisation) signals. Besides the identification of the particle, it is possible to gain information about its energy and momentum, respectively. A variety of detection mechanisms allow to choose the most suitable one depending on the application, e.g. time- or energy-resolution, and the particles of interest. Sometimes it is also useful to employ multi-component detector systems in order to study different particles. In this thesis, a closer look is taken on the detection of muons with scintillators and silicon photomultipliers.

2.1 Scintillators

As mentioned earlier in section 1.3.2, high-energy muons can be detected on Earth. Muons are the most penetrating charged particles as they have almost no interaction with nuclei [17]. The particles ionise or excite matter they go through by electromagnetic interaction with electrons of the molecules. In *scintillators*, the relaxation of these molecules results in the emission of photons in the visible energy range or near that. With a refractive index similar to glass (~ 1.5) the light is more likely to be reflected by the scintillators' walls and captured inside of it [29].

To be useful for particle detection, scintillators should have the following characteristics:

- transparency at the wavelength of the scintillation light

- large efficiency of light production
- short light pulses and little or no delayed light emission
- light emission proportional to deposited energy
- refractive index of about 1.5

It is distinguished between *organic* and *inorganic* scintillators. The application of those is very different as they differ in properties. Organic scintillators consist mostly of atoms with a small Z, which is why their radiation length is rather long. Whereas inorganic scintillators have short radiation lengths due to atoms with high atomic charge. Because of this difference in radiation length, inorganic scintillators are more effective for the detection of X- and γ-rays, whereas organic scintillators are better used for charged particle detection [29].

There are three types of organic scintillators: organic crystals, organic liquids and plastic scintillators. Organic crystals, such as anthracene, are quite expensive in comparison to plastic scintillators. They are, therfore, used less frequently even though they have a large efficiency. Liquid scintillators are mainly used when a large volume is required. They are cheaper than other scintillators and can easily be shifted to another wavelength by adding appropriate materials. However, amongst the organic scintillators, the most used are plastic scintillators. They are made of a polymerisable liquid with usually, chemically speaking, an atomic ring-structure. This base material usually scintillates in the ultra-violet (UV) energy range with an absorption length of only a few millimetres. By adding a wavelength shifter, the absorption length can be extended. The dopant absorbs the UV light and emits photons at a longer wavelength. These can then travel longer through the scintillator before being absorbed. Further, plastic scintillators are quite practical as they are easily produced in every shape required [29].

Another reason, why organic scintillators are useful for the detection of charged particles, is their short decay time (~ns) which leads to a good time resolution. To localise the particle, it is convenient to use several plastic scintillator tiles which are then read out by individual detectors [29].

The company SAINT-GOBAIN produces a few different plastic scintillators with various properties suitable for different energy ranges. They are Polyvinyltoluene-based, are doped with fluorides, have a density of $1.023\,\mathrm{g/cm^3}$ and a refractive index of 1.58. According to SAINT-GOBAIN, they work independently of temperature from -60°C to +20°C [22]. Table 2.1 and figure 2.1 show some properties of *BC-404*, the scintillator used here.

light output	68% of anthracene
rise time	0.7 ns
decay time	1.8 ns
pulse width, FWHM	2.2 ns
wavelength of max. emission	408 nm
light attenuation length	140 cm
bulk light attenuation length	160 cm

Table 2.1: *Scintillation properties of the plastic scintillator BC-404. Light output is given in the percentage of the most efficient scintillator anthracene. Data taken from* SAINT-GOBAIN *data sheet [22].*

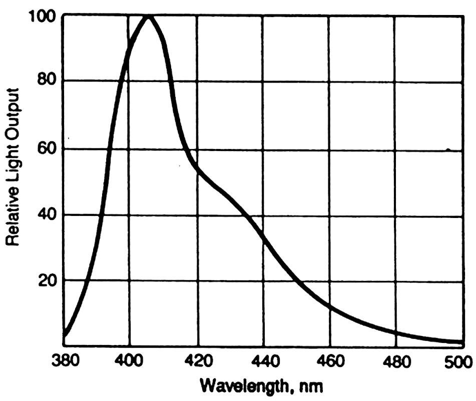

Figure 2.1: *Relative light output versus wavelength of emitted scintillation light for the plastic scintillator BC-404. Wavelength ranges from 380 to 500 nm. Maximum emission at 408 nm. Figure taken from* SAINT-GOBAIN *data sheet [22].*

2.2 Silicon Photomultipliers

The detection of scintillation light is possible with photosensors, e.g. an array of silicon photomultipliers (SiPMs). They can be placed separably at edges and corners of scintillators where the photon density of the scintillated light is higher [23]. Together with a high photon detection efficiency, scintillators are thus a reasonable choice for particle detection.[1] The functionality and some detailed properties of the here-used SiPMs are explained in the following.

A silicon photomultiplier is basically an array of avalanche photodiodes which allow an intrinsically-amplified signal because of avalanches of charger carriers.

[1] *More detailed discussions about the advantages of SiPMs can be found on the* SAINT-GOBAIN *Web Page [23]*

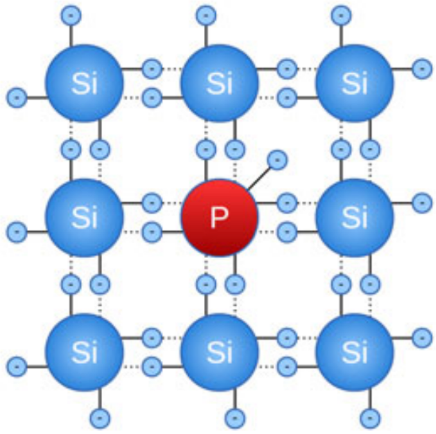

(a) *n-doping with phosphor leads to excess of electrons*

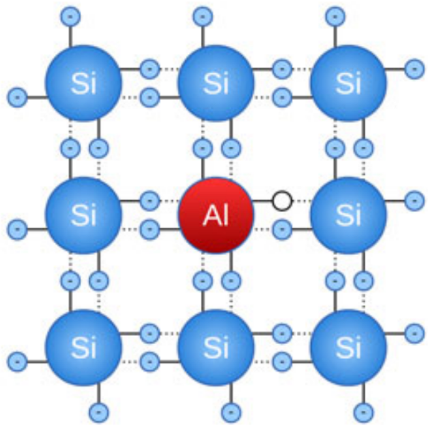

(b) *p-doping with aluminium leads to positive holes*

Figure 2.2: *Schematic illustration of atomic structure of n- and p-doped silicon demonstrates the production of free charge carriers for the current flow. Figure taken from [30, p. 14].*

One diode is build of a p- and a n-doped semiconductor in mechanical contact. *Doping* means to contaminate the crystal structure of a semiconductor with foreign atoms that have a number of valence electrons different to the semiconductor. Thus, a n-doped semiconductor is doped with foreign atoms with more valence electrons, which leads to an excess of electrons and therefore to a potential build-up. Contrarily, for p-doping atoms with less valence electrons are used. The lack of electrons leads to positive holes which cause an opposite potential. Figure 2.2 shows the atomic structure of n-doped (2.2a) and p-doped (2.2b) silicon [30].

When n- and p-doped semiconductors are put in mechanical contact, a gradient of the free charge carriers can be observed. Electrons diffuse and are captured by acceptors or recombine with holes in the p-part and vice versa for holes. The recombination results in a depletion zone of charge carriers between n- and p-layers and different space charge densities. The generated electric field counteracts the diffusion current and causes a potential across the depletion zone. By applying voltage between the ends of the junction, the depletion zone can be influenced [30].

If positive voltage is applied to the p-part (forward bias), the charged particles experience a repulsive force from the equally charged electrodes towards the junction. Hence, the depletion layer becomes thinner and the potential difference smaller. At a sufficiently large voltage the electric field in the depletion zone is so small that it cannot counteract the drift of charged particles any more. The resulting current increases exponentially with the supply voltage [4].

Applying negative voltage to the p-part (reverse bias) has a different effect. The depletion layer becomes larger as the charged particles are attracted to the oppositely charged electrodes. The resulting higher potential barrier prevents the drift of the charged particles to the other layer. This is called *reverse mode*. Although, a very little amount of charge carriers leak through the junction. By applying a sufficiently high voltage, the *breakdown voltage*, free electrons have enough kinetic energy to create more electron-hole-pairs by impact ionisation with valence electrons rather than recombine. Those accelerated electrons can further produce even more electron-hole-pairs. Like this, the number of charge carriers in the depletion zone increases exponentially which is called the *avalanche effect* [4].

If then a photon crosses the depletion region, it creates an electron-hole-pair by being absorbed due to the internal photoelectric effect. The photon is absorbed by an electron which has then enough energy to be excited and leave a positive hole. Due to the reverse biased voltage above breakdown voltage, a single photoelectron can generate an avalanche. The resulting self-sustaining discharge current is called *Geiger discharge*. The change of the external resistance due to recharging is proportional to the incoming amount of light [4, 15]. A schematical illustration of the p-n junction and the effect, that occurs when a particles crosses the depletion zone, is given in figure 2.3.

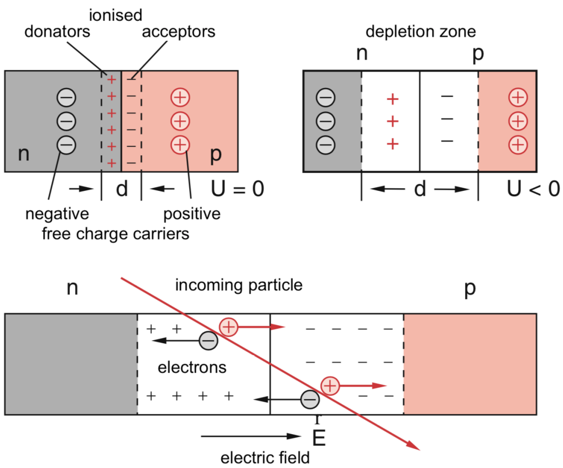

Figure 2.3: *Semiconductor particle detector with p-n junction. By applying negative voltage to the bounds of the p- and n-layers, the depletion zone expands. An incoming particle creates electron-hole-pairs which drift to the different charged sites and generate a signal. Figure taken from [3, p. 96] and modified.*

As mentioned above, the silicon photomultiplier is an array of many parallel avalanche diodes, the *microcells*, connected in parallel to one common cathode and one common anode output. Figure 2.4 shows a sketch and the basic schematic of a SiPM.

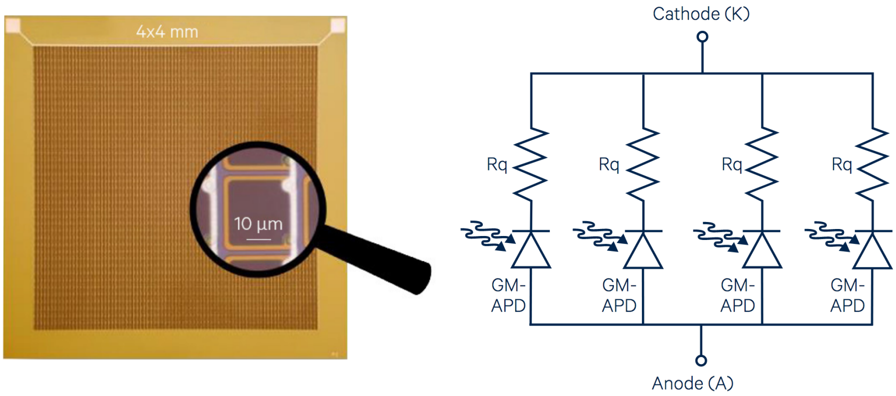

Figure 2.4: *Top view and schematic of a silicon photomultiplier. Microcells are parallel connected to a common cathode and anode. Each microcell consists of a Geiger-mode avalanche photodiode and a quenching resistor connected in series. Figure taken from [5].*

The SiPM signal is a superposition of all microcell signals and represents therefore also the number of fired cells. The pulse signal has an asymmetric shape with a usually short rise time associated with the discharge phase of the diode. The slower falling edge is caused by the recharge time of the diode capacitance [5, 11]. Figure 2.5 shows a typical pulse signal of a SiPM produced by a single photon.

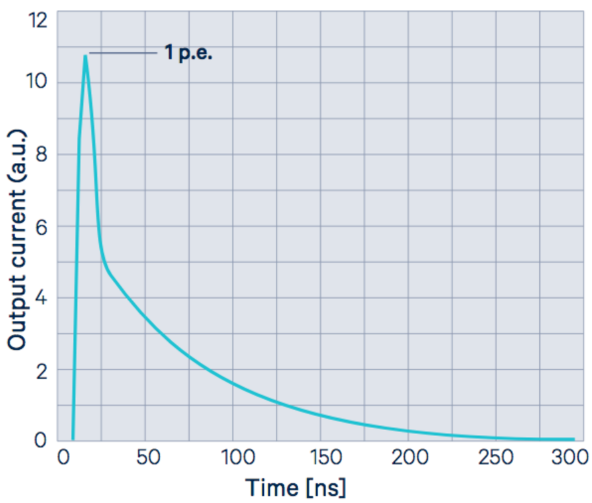

Figure 2.5: *Current pulse produced by a single photon triggering an avalanche in a microcell. The fast rising edge corresponds to the Geiger discharge. The slower falling edge is caused by the recovery phase. Figure taken from [5].*

When analysing the signal, it has to be understood that SiPMs can produce noise. Due to thermic excitations, an electron-hole-pair can also be produced without a photon crossing the sensitive area. The rate of this thermical noise rises exponentially with temperature [30]. Another effect that generates electron-hole-pairs is *crosstalk*. This is caused by induced currents due to firing cells, and thus produced secondary photons in Geiger discharges in neighbour cells. Alternatively, dark counts can be generated by *afterpulsing* when charge carriers generate a delayed signal after being trapped in metastable states. The dark count rate increases with temperature [12, 13, 30].

Other important parameters are the *photon detection efficiency* (PDE) and the *gain*. The former is the ratio of primary Geiger discharges to the number of photons hitting the SiPM and is, therefore, a measure of the SiPM's sensitivity. The latter is a multiplication factor that represents the number of produced photoelectrons in an avalanche. The gain multiplied by the elementary charge e is the amount of charge created by a single cell. Both, PDE and gain, increase with supply voltage. If more photons than the number of microcells hit the sensitive area of the SiPM, saturation can be observed. The microcells that were already hit by a photon cannot generate a new signal while still in recovery [12, 13]. Those dependencies of the here used silicon photomultiplier *PM3315-WB-B0* from the company KETEK are displayed in figure 2.6 and 2.7. KETEK refers here to *over voltage* rather than supply voltage which is the difference of supply voltage and breakdown voltage. The breakdown voltage increases linearly with temperature which is shown in 2.8. A picture and important properties of the SiPM are given in figure 2.9 and table 2.2.

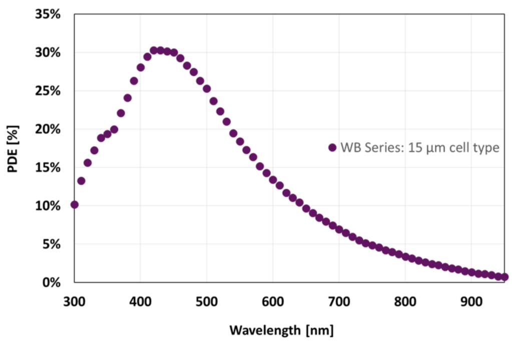

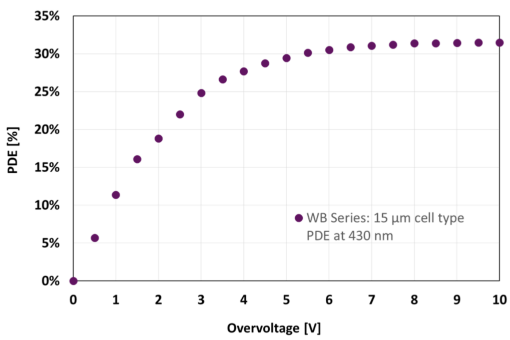

Figure 2.6: *Photon detection efficiency as a function of wavelength at 5 V over voltage (left) and of over voltage (right) at 21° C. Figures taken from* KETEK *data sheet [12].*

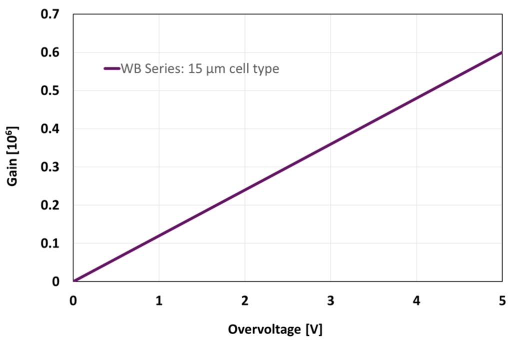

(a) *gain versus over voltage*

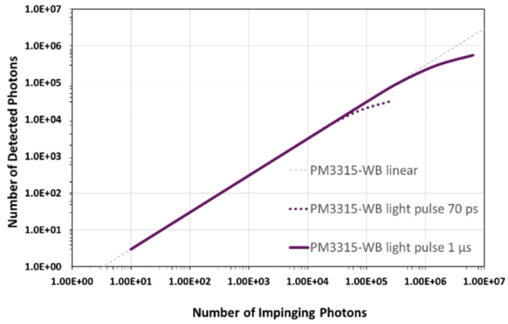

(b) *detected number of photons versus number of impinging photons*

Figure 2.7: *Figures taken from* KETEK *data sheet [12].*

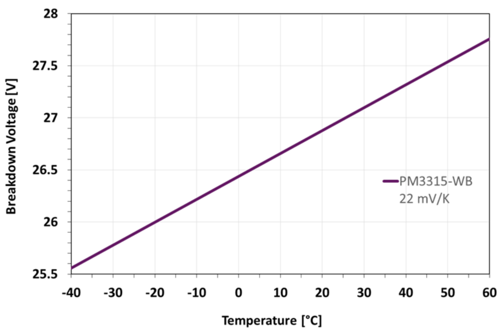

Figure 2.8: *Breakdown voltage versus temperature. Figure taken from* KETEK *data sheet [12].*

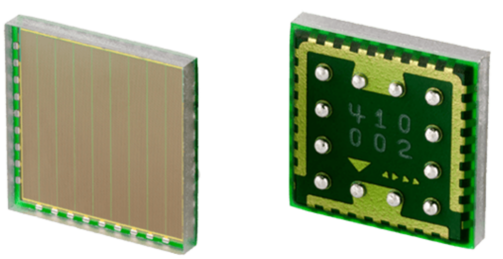

Figure 2.9: KETEK *silicon photomultiplier. Figure taken from [11].*

General Parameters		
active area	$3.0 \times 3.0\,\mathrm{mm}^2$	
microcell size	$15\,\mu$m	
no. of microcells	38800	
Main Characteristics		
breakdown voltage V_{BD} at 21°C	26.9 V	
recommended over voltage V_{OV}	2.0 – 5.0 V	
temperature dependency of V_{BD}	22.0 mv/K	
temperature dependency of gain	0.3%/K at 5.0 V_{OV}	
operating temperature range	−40°C – +60°C	
Performance Overview at 21°C		
	2.5 V_{OV}	5.0 V_{OV}
photon detection efficiency at 430 nm	22%	31%
dark count rate	$50\,\mathrm{kHz/mm}^2$	$100\,\mathrm{kHz/mm}^2$
crosstalk probability	7%	20%
afterpulsing probability	$< 1\%$	
gain	$0.30 \cdot 10^6$	$0.60 \cdot 10^6$
recovery time	13 ns	
signal rise time	< 1 ns	

Table 2.2: *Properties of the* KETEK *silicon photomultiplier PM3315-WB-B0. Data taken from* KETEK *data sheet [12].*

Chapter 3

STRAW-b

STRAW-b (*STRings for Absorption length in Water part b*) is the subsequent mooring line for STRAW that was introduced in the beginning. The main goals are the further investigation of the optical properties of the Pacific Ocean with focus on bioluminescence and the testing of the deployment strategy of strings with a length of 500 m. Before explaining in detail the experiment of most interest for this thesis, the overall concept of STRAW-b is to be explained and a short overview of the other modules is given in the following.

3.1 Concept

Alongside of a 450 m long steel cable, ten glass spheres are mounted at 24 m distance. Each module is electrically connected to a mini junction box, that functions as a power distributor. The connection is done at the bottom via *vertical electrical optical cables* (VEOCs), which have a length ranging of 120 m to 432 m. An anchor keeps the single mooring line at the bottom of the sea at a depth of approximately 2660 m and a buoy on top keeps it vertically floating. A technical drawing of STRAW-b with all its main parts can be seen in figure 3.1.

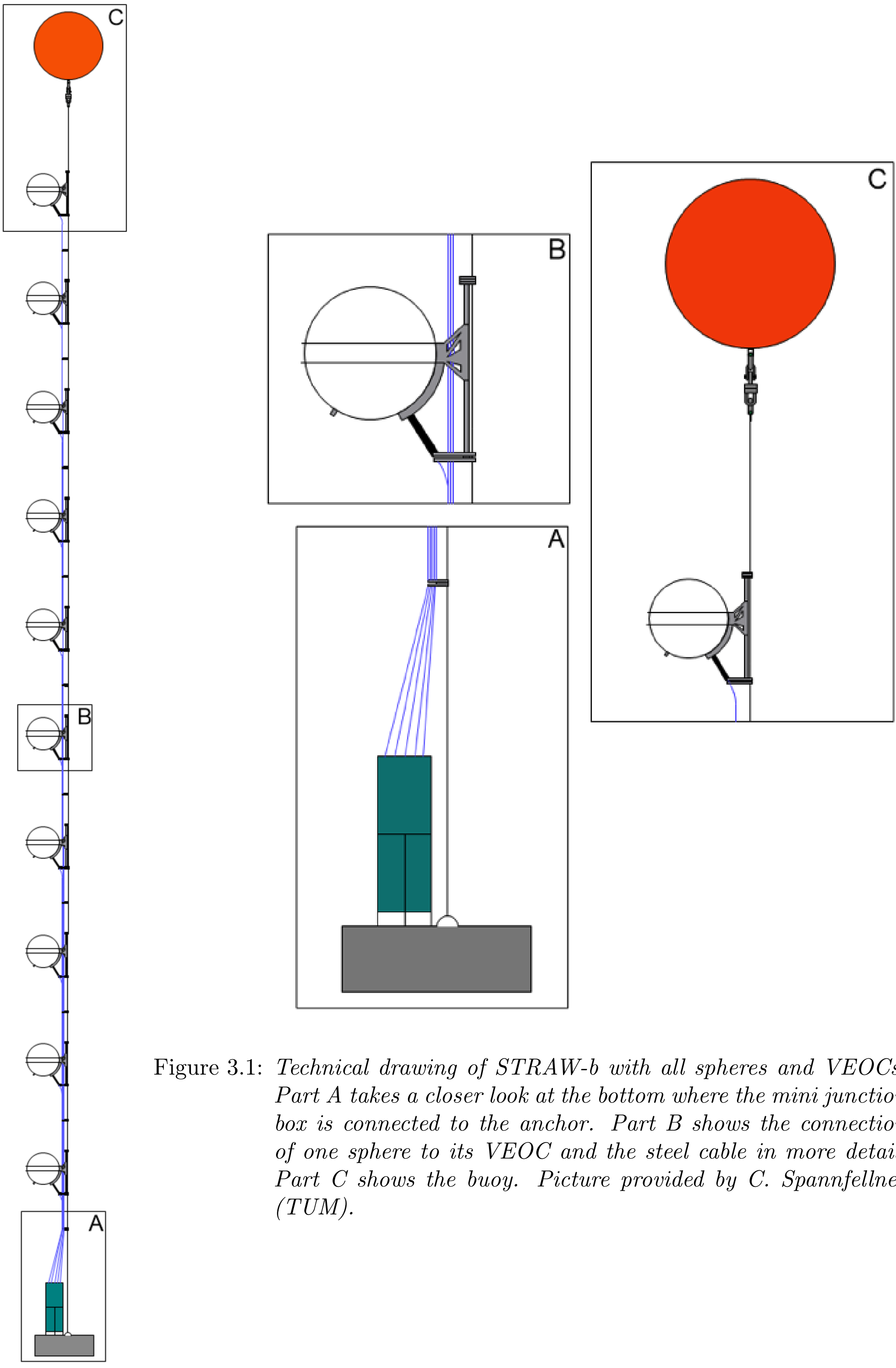

Figure 3.1: *Technical drawing of STRAW-b with all spheres and VEOCs. Part A takes a closer look at the bottom where the mini junction box is connected to the anchor. Part B shows the connection of one sphere to its VEOC and the steel cable in more detail. Part C shows the buoy. Picture provided by C. Spannfellner (TUM).*

3.2 Modules

The modules are installed in 13″ glass spheres with a standard inner mounting. It consists of a metal plate with mounting holes on the top and attached read-out electronics on the bottom. The read-out is done by a *Trigger Readout Board* (TRB3sc) and a PaDiWa3, which supports 16 channels and has a time resolution of $< 20\,\mathrm{ps}$.[1] The modules are provided with 48 VDC and Ethernet via the VEOC and are equipped with an Odroid-C2 computer.[2] Moreover, the standard module contains pressure, temperature, humidity, tilt and magnetic field accelerometer sensors. Figure 3.2 shows a technical drawing of the preliminary standard sphere with inner and outer mounting.

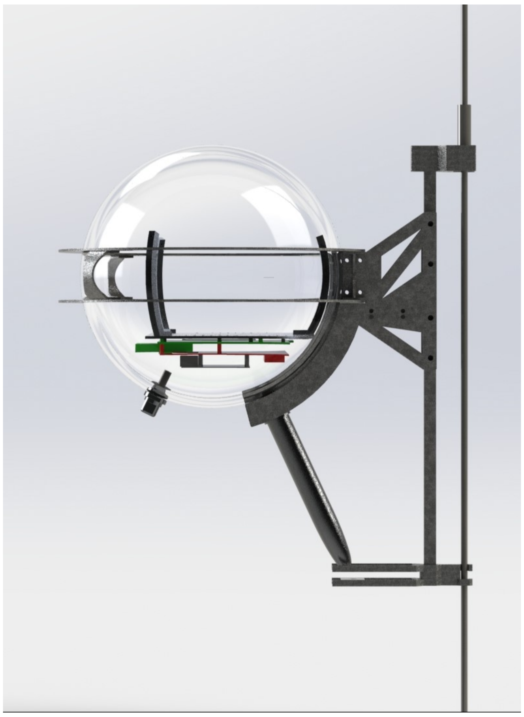

Figure 3.2: *Technical drawing of the preliminary standard sphere for STRAW-b modules. Attached to the glass sphere are the standard outer and inner mounting with read-out electronics. Picture provided by C. Spannfellner (TUM).*

Being a pathfinder for a future telescope, STRAW-b is planned to give information whether all instruments stay intact in the ocean. Currently, five standard modules and five specialised modules are planned. With the standard module information about pressure, temperature and humidity inside the spheres is gained.

The specialised modules have, in addition to the standard setup, specialised instruments for different purposes. One of those is a LiDAR (*Light*

[1] *TRB3sc and PaDiWa3 are both developed by GSI Darmstadt [18]*

[2] *The Odroid-C2 is a 64-bit quad-core single board computer, further information in [9]*

Detection And Ranging), which will measure the absorption length and scattering properties at Cascadia Basin complementing the STRAW measurements.[3] To record bioluminescence spectra emitted by pyrosomes, three different spectrometers are in the planning. Those living organisms emit light in flashes when stimulated mechanically or electrically [27]. To capture those photonic stimuli, an astronomy camera with an 11 Mega pixel resolution is planned to be deployed with the spectrometers.

The focus of this thesis lies in in the last specialised module, a devise to track muons. The development and first test data of this muon tracker will be discussed in detail in the next chapter.

[3] *Details on first results of the STRAW data can be found in [1]*

Chapter 4

Muon Tracker

The basic idea of the muon tracker module is the detection of atmospheric muons in the Pacific Ocean. First, the development of a feasibility study for the instrument is outlined in this chapter. Then, the design of the module and finally, calibration measurements and first results of muon detection in the laboratory are presented in the following.

4.1 Feasibility Study

For the development of this particle detector, calculations of the expected muon flux in the deep sea and the energy deposit in the scintillator have been made and are explained below. Further, estimations about the light yield and the detection with silicon photomultipliers are presented.

4.1.1 Expected Muon Flux

Due to interaction with matter, the muon flux decreases underground or underwater with increasing depth. The KM3NeT (*KM*^{3}*-scale Neutrino Telescope*) collaboration used two detectors in the deep of the Mediterranean Sea to develop a muon intensity function depending on the depth. Each detector consists of a three dimensional array of Digital Optical Modules (DOMs). A DOM is a glass sphere with a number of photomultipliers that detect Cherenkov light emitted by high-energy charged particles passing through water. To distinguish between muons and other charged particles, only events when eight or more PMTs were hit in a coincidence are counted. Bioluminescence and ^{40}K background can then be excluded. The difference in depth of those DOMs results in the measurement of different rates. The formula developed with this data is given in 4.1. Here, the muon intensity $I_\mu(d)$ at a depth d is the fraction of the vertical flux $I_\mu(d, \theta = 0)$ and $C(d)$, a factor that accounts for angular integration [14].

$$I_\mu(d) = \frac{I_\mu(d, \theta = 0)}{C(d)} = \frac{A_1 \cdot e^{A_2 \cdot d} + A_3 \cdot e^{A_4 \cdot d}}{B_1 + B_2 \cdot d} \tag{4.1}$$

$$A_1 = 1.31 \cdot 10^{-5}\,\mathrm{cm^{-2}s^{-1}sr^{-1}},\ A_2 = -2.91 \cdot 10^{-3}\,\mathrm{m^{-1}},$$
$$A_3 = 7.31 \cdot 10^{-7}\,\mathrm{cm^{-2}s^{-1}sr^{-1}},\ A_4 = -1.17 \cdot 10^{-3}\,\mathrm{m^{-1}},$$
$$B_1 = 4.16 \cdot 10^{-1}\,\mathrm{s^{-1}},\ B_2 = 1.07 \cdot 10^{-4}\,\mathrm{m^{-1}s^{-1}}.$$

As the STRAW-b modules operate at depths between approximately 2200 and 2660 m, the expected muon flux, calculated with formula 4.1, is 5 to $10 \cdot 10^{-8}\,\mathrm{cm^{-2}s^{-1}}$ or about 50 to $100\,\mathrm{m^{-2}d^{-1}}$. Similar results were achieved in e.g. [2].

4.1.2 Energy Loss in Scintillator

As explained in chapter 2, scintillators emit light when a passing muon deposits some of its energy. The amount of this energy can be calculated with formula 1.2. The SAINT-GOBAIN scintillator *BC-404* has a density ρ of $1.023\,\mathrm{g/cm^3}$. The ratio of hydrogen and carbon atoms is 1.107 [24] which means 52.54% H and 47.46% C. The effective atomic number Z_{eff} and atomic weight A_{eff} can be calculated with respect to the fraction of C ($Z = 6$, $A = 12$) and H ($Z = 1$, $A = 1$):

$$Z_{\text{eff}} = 0.4746 \cdot 6 + 0.5254 \cdot 1 = 3.373$$
$$A_{\text{eff}} = 0.4746 \cdot 12 + 0.5254 \cdot 1 = 6.221$$

The mean excitation potential is calculated with formula 1.4 to $I = 47.8\,\mathrm{eV}$. The maximum energy transfer in a single collision can be calculated with formula 1.3. We are here interested in muons with energies ranging from approximately 1 to 100 GeV (figure 1.4). For a muon ($m_\mu = 105.658\,\mathrm{MeV}$ [28]) with an energy of 1 GeV, the maximum energy transfer is $W_{max} = 82.9\,\mathrm{MeV}$. By using these values, the mean energy loss in the *BC-404* scintillator is calculated to

$$-\mathrm{d}E/\mathrm{d}\tilde{x} \approx 2.48\,\mathrm{MeV\,cm^{-1}}. \tag{4.2}$$

To identify whether this is detectable with the scintillator, the value of the minimum energy deposit that is needed for ionising, and therefore light emission needs to be calculated. In plastic scintillators, the minimum ionising value of $-\mathrm{d}E/\mathrm{d}x$ is approximately $1.90\,\mathrm{MeV\ g^{-1}\ cm^2}$ [16]. This means with a density of $1.023\,\mathrm{g/cm^3}$ an energy deposit of

$$\begin{aligned}
\mathrm{d}E/\mathrm{x} &= \frac{\mathrm{d}E}{\mathrm{d}x} \cdot \rho \\
&= 1.90\,\frac{\mathrm{MeV\,cm^2}}{\mathrm{g}} \cdot 1.023\,\frac{\mathrm{g}}{\mathrm{cm^3}} \cdot x\,\mathrm{cm} \\
&\approx 1.94\,\mathrm{MeV\,cm^{-1}}.
\end{aligned}$$

Together with the value from equation 4.2, the scintillator *BC-404* seems suited for the detection of atmospheric muons.

4.1.3 Coincidence

Also other charged particles than muons deposit energy in scintillators and could, therefore, trigger an unwanted signal. To distinguish between background radiation and muons, commonly only coincident signals in two different scintillators are counted as muon events. The gamma ray is completely absorbed in the photoelectric effect and pair production processes. It can deposit a fraction of its energy through Compton scattering [16]. An exemplary coincident pulse signal is shown in figure 4.1. The time difference Δt of the peaks represents the distance d that the muon travels from one scintillator to another with velocity c/n, n being the refractive index ($n_{\mathrm{air}} = 1$).

$$d = \frac{c}{n} \cdot \Delta t$$

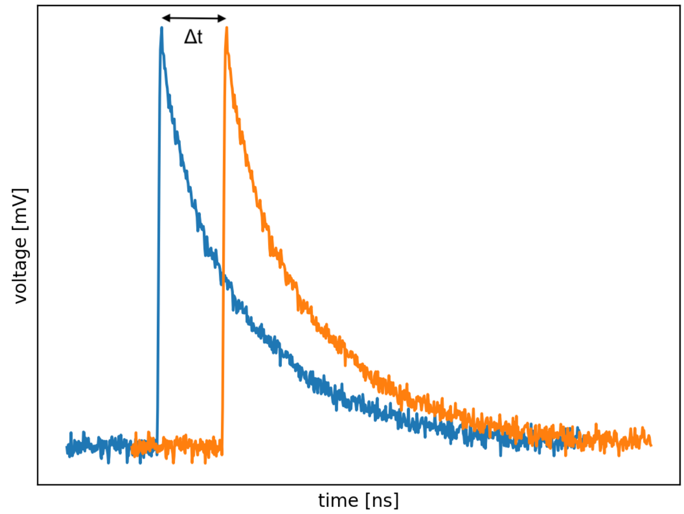

Figure 4.1: *Exemplary coincident pulse signal with time difference Δt.*

4.1.4 Position Reconstruction

To obtain information about the incident angle of the muon, the position of the interaction with the scintillator has to be reconstructed. This can be done by dividing the scintillator in several tiles or by dual ended read-out. With the former the scintillator tiles work as "pixels" and are individually connected to detectors. For the latter good time resolution is required as the position of the incident particle in the scintillator is reconstructed by comparing the rise time of the pulse signals. Additionally, the different measured intensities give information about which photosensor has detected more light, and hence was closer to the crossing muon. A combination of both seems beneficial.

4.1.5 Scintillator Size

In order to determine a suitable size of the scintillators for the experiment, those considerations and calculations have to be taken into account. Figure 4.2 shows the expected coincidence rate in two scintillators and the maximum measurable incident angle θ_{max} depending on the total side length of squared scintillators and the distance between them. The angle is measured from the centre axis.

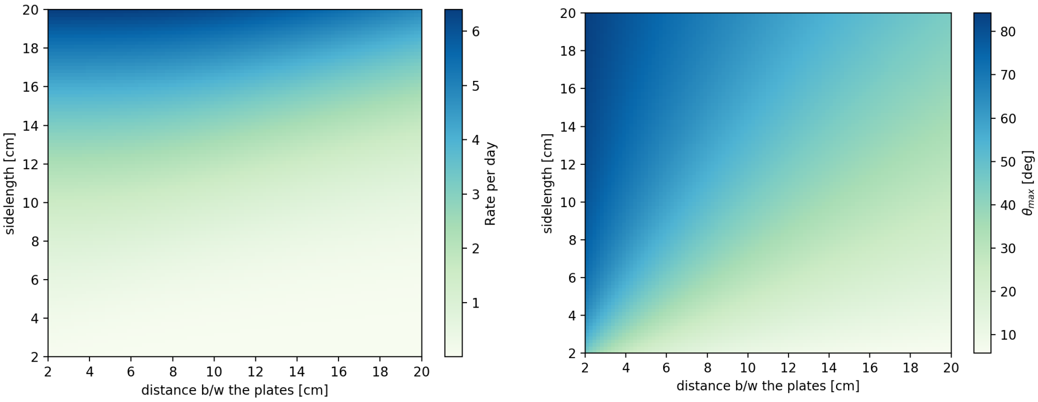

Figure 4.2: *Expected muon rate (left) and θ_{max} (right) depending on the size of the scintillators and the distance between them. Plots developed with the help of Na. Khera (TUM).*

It is evident that the muon rate and also θ_{max} scale up with an increasing side length as well as with a decreasing distance between the plates. Those dimensions are limited by the given space within the sphere.

4.1.6 SiPM Configuration

In order to prevent the scintillation light of escaping the scintillator undetected, reflective material is added to the surfaces [21]. SiPMs can then be placed in left-open holes. The trapped photons are then either refelcted to the detector or absorbed after travelling a certain distance in the scintillator. In order to collect as much light as possible, the SiPMs should be placed at edges or near corners of the scintillator as the photon density is highest there. With an array of SiPMs the fraction of the covered surface and, hence, the light collection efficiency can also be increased [23].

4.1.7 Light Output

The light output of the scintillator is 68% of the light output of anthracene which needs an energy deposit of 60 eV to create one photon [16]. Thus, approximately 88 eV are needed in the scintillator to emit one photon. That means, for a 1 GeV muon that deposits 2.48 MeV/cm about $2.8 \cdot 10^4$ photons/cm are emitted. The emission wavelength is in the range 380 to 500 nm. Scintillator values are taken from figure 2.1 and table 2.1. The percentage of those photons that hit the sensitive area of a SiPM is dependent on the fraction of the surface covered by the SiPM, the incident angle of the muon and the reflectivity of the surfaces.

In [21] they compared the number of detected photons with the total number that were created by a 1 MeV electron beam in a plastic scintillator. They used three different sizes of scintillators with a volume of $(F \times L)^3$ with $L = 2\,\mathrm{cm}$ and $F = 1, 3, 10\,\mathrm{cm}$, respectively. A TiO_2 coating was used on all sides for better reflectivity. The detector had a width of 1 cm. Their results were approximately 70, 12 and 0.8% for the three different sidelengths.

For further calculations, assumingly about 12% of the $2.8 \cdot 10^4$ photons are reflected to the SiPM. The photon detection efficiency of the *PM3315-WB-B0* SiPM at 5 V over voltage and 430 nm is 31%. Therefore, those approximations result in roughly $0.12 \cdot 0.31 \cdot 2.8 \cdot 10^4 \approx 1000$ photons that generate an avalanche. Multiplied with a gain of $0.60 \cdot 10^6$ leads to approximately $0.6 \cdot 10^9$ photoelectrons. (SiPM values are taken from table 2.2.) The produced charge is

$$Q_{\mathrm{pulse}} = 0.6 \cdot 10^9 \cdot 1.6 \cdot 10^{-19}\,\mathrm{C} \approx 10^{-10}\,\mathrm{C}.$$

4.2 Module

In this section the final experiment setup as well as calibration measurements are presented and discussed.

4.2.1 Experimental Setup

The muon tracker module is designed to fit in the given parameters of the standard module. Limitations are given by space and read-out electronics. The developed design combines the requirements of a large area covered by scintillators and a distance of those which is within the possible time resolution.

The module consists of two housing boxes connected with threaded bars at a distance of 10 cm. One housing box compromises a Polytetrafluorethylen (PTFE or "teflon") frame with outer dimensions $17.0 \times 17.0 \times 21.5\,\mathrm{cm}^3$ and two 1 cm thick Aluminium plates. Reflective foil is placed between the scintillators and the aluminium plates. In each box is an array of 2×2 *BC-404* scintillator tiles separated by 6 mm thick teflon walls within the box. The dimensions of one tile are $7.5 \times 7.5 \times 2.0\,\mathrm{cm}^3$. The light output of the scintillators is read out by *PM3315-WB-B0* SiPM arrays. Holes for them in the Aluminium plates are near one corner of each scintillator on top and bottom, respectively. Altogether there are 16 SiPM arrays, two for each scintillator. Always four SiPM arrays are connected on one printed circuit board (PCB). Figure 4.3 shows a schematic drawing of the top view of one housing box and figure 4.4 a picture of the complete setup.

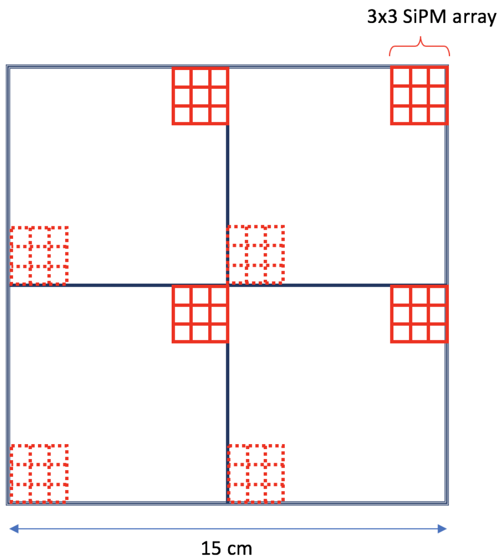

Figure 4.3: *Schematic drawing of top view of housing SiPM arrays on top (continuous lines) and on bottom (dashed lines). Picture provided by Na. Khera (TUM).*

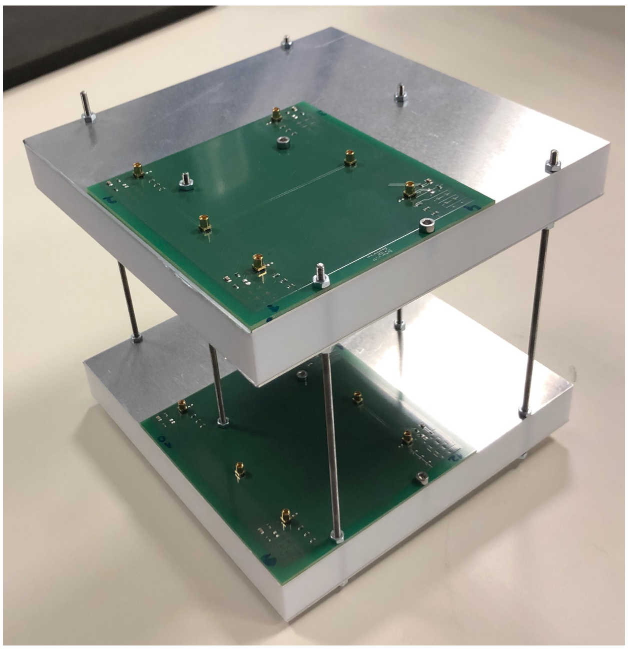

Figure 4.4: *Picture of the muon tracker setup which contains two housing boxes connected by threaded bars, eight scintillator tiles within those and four PCBs.*

Scintillators

The size of the scintillators is a compromising solution between the coincidence rate, the angle $\theta_{\max}$ and the distance between the top and the bottom layer. With the time resolution of the *PaDiWa3* (20 ps) a distance of approximately 10 cm seems reasonable. The muon would need at least

$$t = \frac{0.1\,\mathrm{m}}{c} \approx 300\,\mathrm{ps}$$

to travel from one layer to the other. This is 15 times the resolution, and hence estimated to be analysable with the given read-out electronics. This could not have been tested yet as the electronics have not been finalised at the time of this thesis.

With a distance of 10 cm between top and bottom layer, the side length is limited by the sphere to approximately 15 cm. This results in an estimated detection rate of about 3 muons a day and a θ_{max} of approximately 55° (figure 4.2).

As mentioned earlier, the reconstruction of the incident angle can be done by dividing the scintillators in tiles. The design of two 2×2 arrays is based on the limitation of 16 read-out channels. Like this, two SiPM arrays can be put on each of the eight scintillator tiles. By knowing which tile was hit, the incident direction can already be narrowed down to one of four sectors. Thanks to using a dual read-out system the event should be visible with both detectors. By comparing the two signals the position within one scintillator and therefore, the approximate angle can be investigated.

Housing

The Housing serves as mounting as well as reflector of the emitted light of the scintillators. The choice of material is based on reflectivity measurements and is explained further in following.

Teflon Frame and Reflective Foil As mentioned before, the light collection efficiency increases, if the scintillator is wrapped in reflective material. Diffuse reflecting teflon is an often used choice as e.g. in [26]. Specular reflecting foil might also be beneficial because of a very high reflectivity. The transmission and the reflectivity of normal and optical teflon with different thickness and of reflective foil have been measured with a spectrometer. The samples of normal teflon had 1.0, 2.0 and 3.0 mm thickness and of optical teflon had 0.5, 1.0, 1.5 and 2.0 mm. The reflective foil sample was 50 μm thick. A light beam of a certain wavelength ranging from 250 to 500 nm was targeted at the samples. A reference spectrum was taken with a teflon spectralon which unfortunately was impure. Therefore, the data points have an estimated uncertainty of 2.5%. The transmission spectrum and the reflection spectrum are shown in figure 4.5 and 4.6, respectively. The wavelength region of interest is here 380 – 500 nm as this is the light output range of the scintillator (figure 2.1).

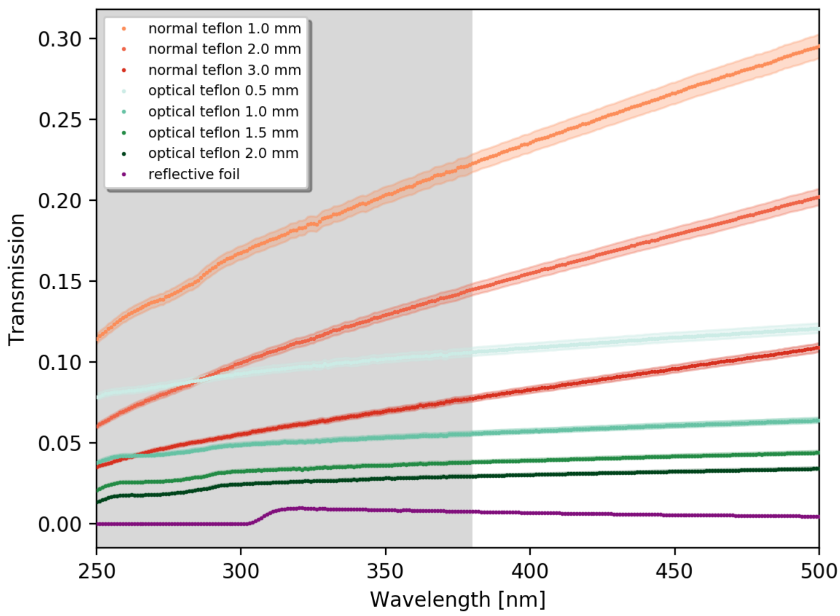

Figure 4.5: *Transmission spectrum of normal and optical teflon with different thickness and of reflective foil. Bands around data points mark estimated uncertainties of 2.5% caused by the reference spectrum of an impure spectralon. Wavelength ranges from 250 to 500 nm. Grey region marks wavelength range of less interest in this case.*

The measured transmission spectrum shows that the fraction of through coming light is strongly dependent on the thickness of the material. For normal teflon a difference of 1 mm in thickness results in up to 10% variation of transmission. This variation becomes less with increasing thickness of the material which can be observed by comparing the curves of optical teflon. It is further evident that the normal teflon is the most penetrable and the reflective foil the least. However, the transmission of normal teflon with a sufficiently large thickness is comparable to a thinner sample of optical teflon. Reflective foil has a transmission of only a few percent.

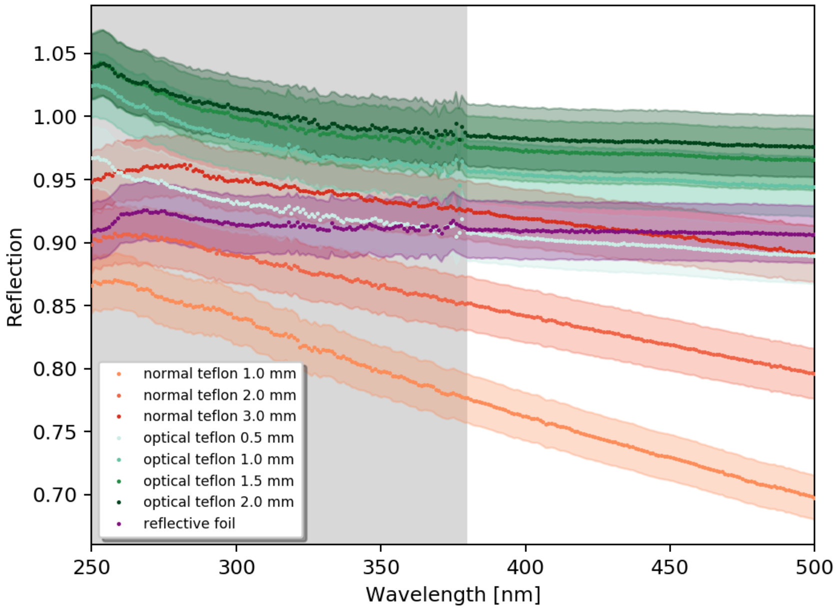

Figure 4.6: *Reflection spectrum of normal and optical teflon with different thickness and of reflective foil. Bands around data points mark estimated uncertainties of 2.5% caused by the reference spectrum of an impure spectralon. Wavelength ranges from 250 to 500 nm. Grey region marks wavelength range of less interest in this case.*

The reflection spectrum shows also the dependency on the thickness of the material. The highest reflectivity was measured for 2 mm optical teflon. That, and also the 1.5 and 1.0 mm sample, reflected even more light than the reference sample as can be seen in the low wavelength region where values are above 100%. In accordance with the results of the transmission spectrum, the normal teflon has the least reflectivity. Nevertheless, this can be improved with a greater thickness.

Additionally optical teflon is rather expensive. That is why, for the frame normal teflon with a thickness of 6 mm is used. Reflective foil is placed on the top and bottom side. With this combination of diffuse and specular reflection the light output is enhanced.

Figure 4.7 shows a technical drawing with dimensions of the teflon frame and a picture within the module.

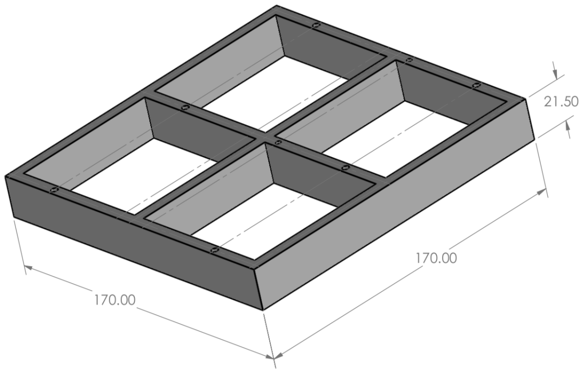

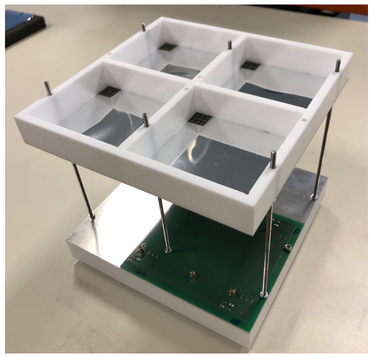

Figure 4.7: *Technical drawing and picture of teflon frame.*

Aluminium Plates On top and bottom of the frame are 1 mm thin aluminium plates on which the PCBs are mounted. They have holes for the SiPM arrays near each corner of the scintillators. Figure 4.8 shows a technical drawing with dimensions.

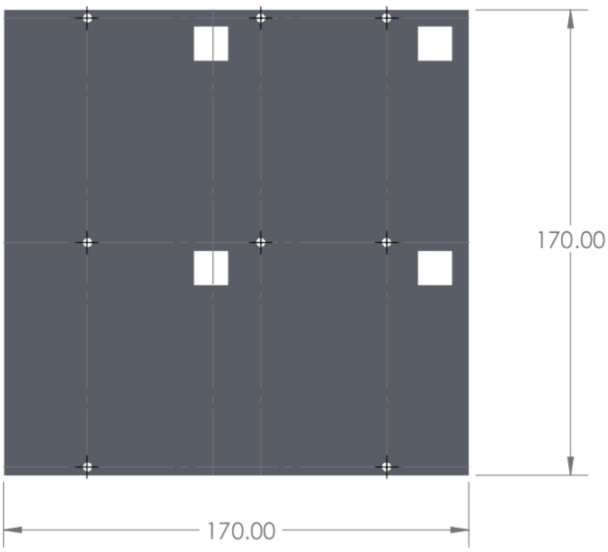

Figure 4.8: *Technical drawing of aluminium plate with squared holes for SiPM arrays and drill holes for mounting screws.*

SiPMs

On each side of the housing are PCBs ($106 \times 110\,\mathrm{mm}^2$) with four SiPM arrays in the corners. Each array consists of nine $3 \times 3\,\mathrm{mm}^2$ SiPMs and has its own signal output pin. Those can be connected individually to the 16 channels of the read-out electronics on the bottom of the sphere that were mentioned in chapter 3. A Picture of the PCB and the SiPM array is given in 4.9.

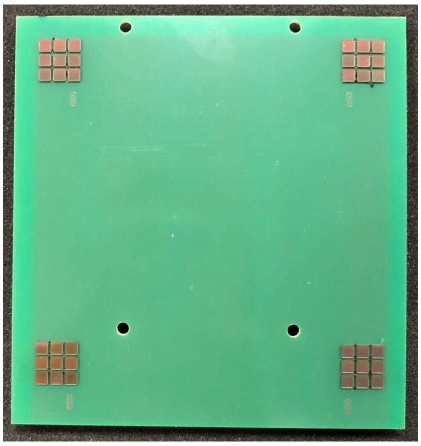
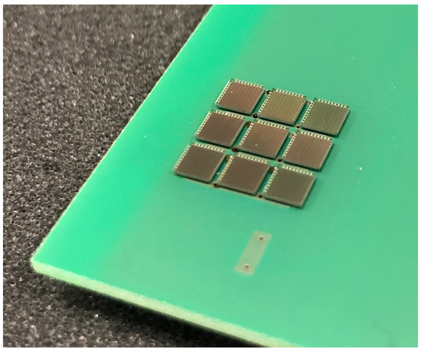

Figure 4.9: *Printed circuit board with four* 3×3 *SiPM arrays and drill holes for mounting screws. Dimensions of PCB are* $106 \times 110\,mm^2$.

Characterisation measurements of the SiPM arrays are presented in the next chapter.

4.2.2 Characterisation Measurements of SiPM Arrays

In order to be able to compare the pulse signals of the 16 SiPM arrays, characterisation measurements have been made. For that, the PCBs were put in a dark box together with a flashing light source. The PCBs were connected to a power source and the signal was read-out by an oscilloscope. Data was taken individually for each array within the same setup at different supply voltages. Those were approximately 1 to 5 V above breakdown voltage of the SiPMs: 29, 30, 31 and 32 V. One thousand waveforms were measured for each voltage for each array.

The oscilloscope measures the created output current

$$I = \frac{\mathrm{d}Q}{\mathrm{d}t} = \frac{U(t)}{R} \tag{4.3}$$

when photons hit the SiPM array and uses a termination resistor $R = 50\,\Omega$. The pulse signal is pictured in voltage over time. Figure 4.10 shows one exemplary measured pulse signal.

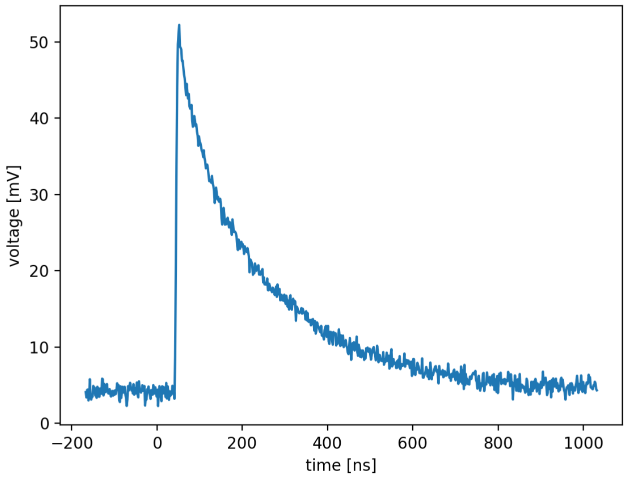

Figure 4.10: *Measured pulse signal of a SiPM array.*

Intensity

For the evaluation of the data, each measurement was analysed individually at first. The value of the area $\int U(t)\,\mathrm{d}t$ under the curve was calculated for the 1000 waveforms of one measurement and put in a histogram. The mean value of one measurement was then investigated with a gaussian fit. In figure 4.11 exemplary characterisation plots of one array at supply voltage 32 V are presented. The picture on the left (4.11a) shows the histogram of the calculated area and on the right (4.11b) the fit curve.

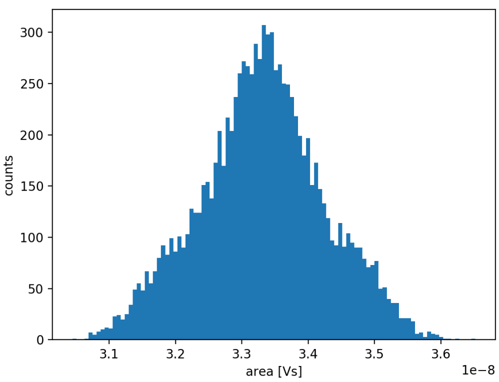

(a) *histogram of calculated area $\int U(t)\mathrm{d}t$ of 1000 waveforms*

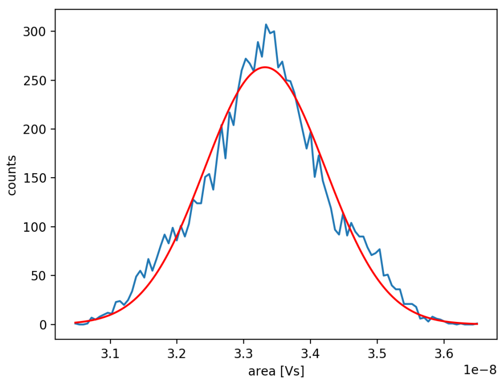

(b) *gaussian fit of histogram in order to investigate mean value of the area*

Figure 4.11: *Exemplary characterisation plots for one measurement of SiPM pulse signals.*

Like this, mean values of the area were calculated for each measurement, i.e. for 16 SiPM arrays at four different supply voltages.

With equation 4.3 it is evident that the area under the curve

$$\int U(t)\,\mathrm{d}t$$

is proportional to the total charge that was created

$$Q_{\text{pulse}} = \frac{1}{R}\int U(t)\,\mathrm{d}t.$$

The value of $q_{\text{pulse}} \equiv Q_{\text{pulse}}/e$, here called *intensity* of one pulse, represents the number of photoelectrons gained by the whole array when illuminated with the same light pulse. With a photodiode the approximate number of photons per pulse was investigated to be around $1.3 \cdot 10^5$. The intensity for each measurement is displayed in figure 4.12.

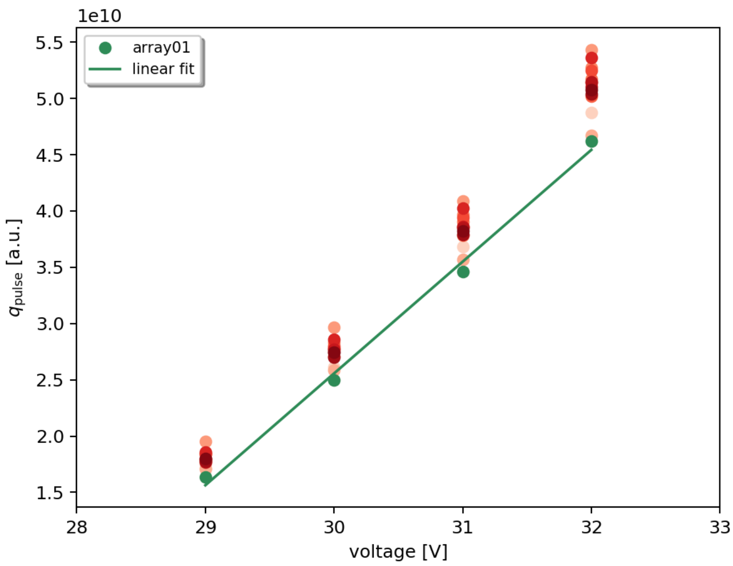

Figure 4.12: *Values of q_{pulse} for 16 SiPM arrays at four different supply voltages. Shades of red represent arrays. Error bars are smaller than markers. Linear fit and data points of one array are green.*

The linear increase of the intensity with supply voltage is demonstrated with a linear fit curve of the data points from one arbitrarily chosen array, called *array01*. The fit curve is $[(0.99 \pm 0.05) \cdot U - (27.2 \pm 0.2)\,\mathrm{V}] \cdot 10^{10}$.

If divided by the number of photons ($\sim 10^5$), the intensity values ($\sim 10^{10}$) are comparable to the given values of the gain of a single SiPM ($\sim 10^5$) (figure 2.7a).

Multiplication Factor

As mentioned above, those characterisation measurements were made in order to compare the signal response of the different SiPM arrays. For that, all values of q_{pulse} were divided by that of *array01*, at 29 V supply voltage. Hence, the fraction represents a multiplication factor of data from an array $i = 01, 02, ...16$ at supply voltage U in comparison to the data of *array01* at 29 V and is defined as

$$f_{i,\,U} \equiv \frac{\text{intensity of array } i \text{ at voltage } U}{\text{intensity of } \textit{array01} \text{ at } 29\,\text{V}} = \frac{q_{\text{pulse},\,i,\,U}}{q_{\text{pulse},\,01,\,29\,\text{V}}}.$$

Values of $f_{i,\,U}$ for all measurements are displayed in figure 4.13.

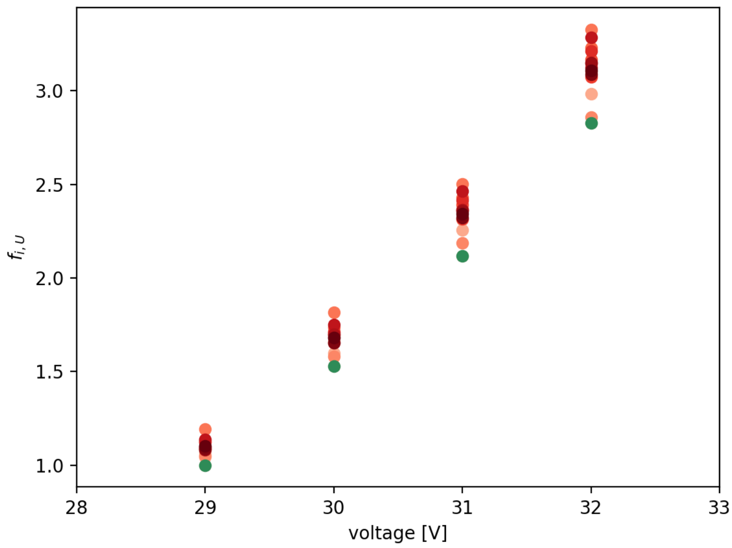

Figure 4.13: *Fraction of intensity values at different supply voltages between all arrays and array01 (green) at 29 V. Shades of red represent arrays.*

Obviously, the multiplication factor increases with supply voltage as the intensity does. Values at 29 V are around 1.0 and scale up to around 3.0 at 32 V. The figure shows further, that also the range of the value for the different arrays increases with supply voltage. While, the maximum variation at 29 V is approximately 20%, it goes up to about 50% for 32 V. This is caused by small differences in the gain at lower voltages resulting in increased differences at higher due to the linear dependency of the gain on over voltage (see figure 2.7a).

With the gained information of multiplication factors measured data is now comparable. When analysing SiPM array signals, measured data will be divided by the respective value of $f_{i,\,U}$.

Temperature Dependency

As STRAW-b will be deployed in a cold environment (2°C) [1], the temperature dependency of the module is relevant. On the one hand, the scintillators work independently of temperature, on the other hand, the SiPMs are strongly affected due to being semiconductors (see chapter 2).

In order to investigate the temperature dependency of the SiPM arrays, the same characterisation measurements were made in a cooled setup. The fraction of the intensity of an array i at supply voltage U at approximately 10°C and the intensity of *array01* at 29 V at room temperature were calculated. Values of $f_{i,\,U}$ at for all measurements are displayed in figure 4.14.

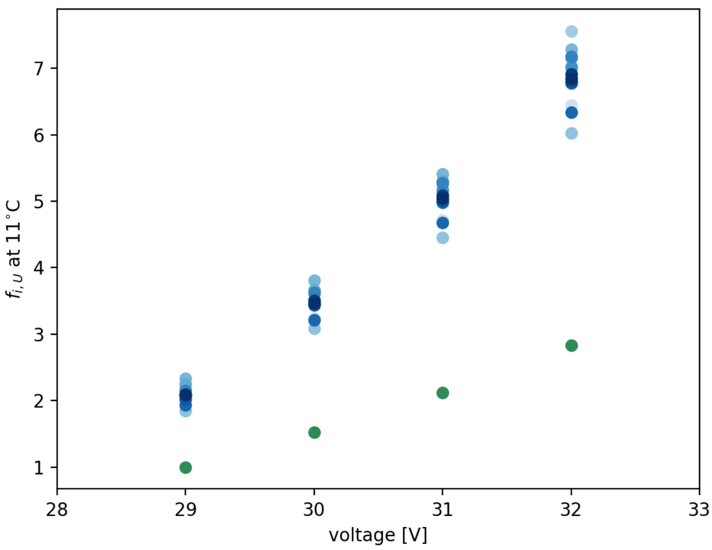

Figure 4.14: *Fraction of intensity values $f_{i,\,U}$ at different supply voltages between all arrays at 10°C and array01 (green) at 29 V at room temperature. Shades of blue represent arrays.*

In comparison to the values at room temperature, the multiplication factor is significantly increased. This means that the intensity was higher at lower temperatures. Therefore, a larger current was measured by the oscilloscope. This is due to a decreased breakdown voltage at lower temperatures (figure 2.8) which results in a larger over voltage for constant supply voltage. The gain increases with over voltage (figure 2.7a), and therefore $f_{i,U}$ is higher.

As mentioned earlier, this dependency is linear in the considered voltage range. As the breakdown voltage is also linear dependent on temperature, it can be assumed that q_{pulse} decreases linearly with increasing temperature:

$$V_{\text{BD}} \propto T \qquad V_{\text{OV}} = V - V_{\text{BD}}$$
$$\rightarrow q_{\text{pulse}} \propto V_{\text{OV}} \propto -V_{\text{BD}} \propto -T.$$

Figure 4.15 shows q_{pulse} of all measurements as a function of temperature. The temperature has an estimated uncertainty of ±2°C at room temperature. For the measurements at lower temperature the uncertainty is approximated with +3°C and −1°C as the setup was in a warm environment.

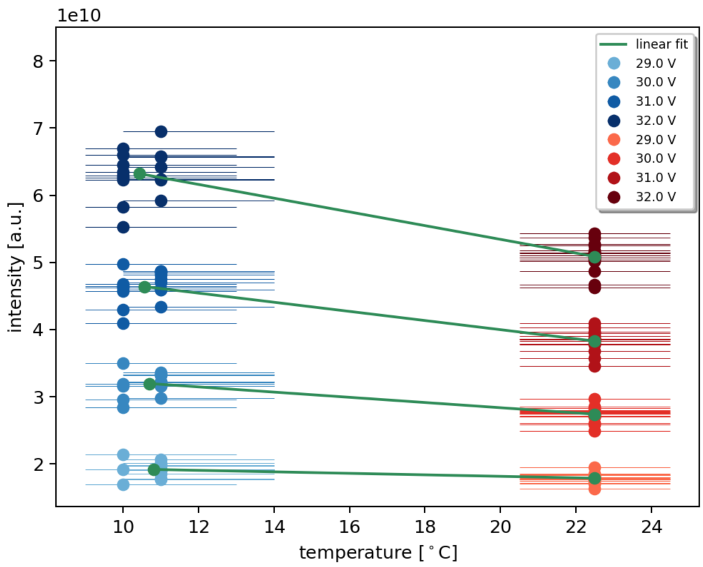

Figure 4.15: *Values of q_{pulse} for different supply voltages as functions of temperature. Error bars show uncertainty of temperature.*

The decreasing behaviour of q_{pulse} is evident. The linearity of the fit curve is obvious as only two data points are taken into account, respectively. In order to develop an appropriate function a third measurement is at least needed.

4.2.3 Proof of Concept

The muon tracker was tested in the laboratory in a dark box. For that, only one of the top sintillators and one of the bottom scintillators were considered. The two SiPM arrays of both scintillators were connected to an oscilloscope. One of the coincident signals, that were measured, is shown in figure 4.16.

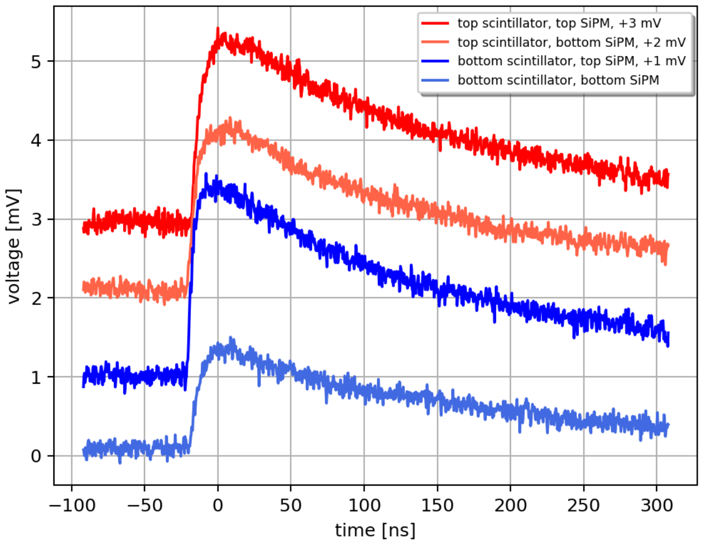

Figure 4.16: *Coincident signal in two scintillators detected by two SiPM arrays each. For better distinguishability are three of the curves shifted by 1.0, 2.0 and 3.0 mV, respectively.*

The values were divided by the respective factor $f_{i,U}$, and are therefore comparable. It is visible that the top SiPM arrays of both scintillators detected more light than the bottom arrays. Assumingly, the muon was closer to those arrays when crossing the scintillators, respectively. With a better time resolution, it would also be visible which scintillator was hit first.

Summary and Conclusions

This thesis has presented the development of a muon tracker as a specialised module in a glass sphere for *STRAW-b*, a pathfinder of a new large neutrino telescope, namely *P-ONE*. First measurements in the laboratory have shown that the detection of atmospheric muons is possible with the setup.

After a detailed discussion about the expected muon flux and the energy loss in the scintillator, the possibility of distinguishing muons from other charged particles and of gaining information about the incident direction has been studied. Further, the configuration of photosensors, here silicon photomultiplier arrays, and the possible light detection efficiency with those have been outlined.

The results of this feasibility study have been presented with the final design of the module. The size and quantity of the scintillators and the SiPM arrays was developed in consideration of limitations given by the dimensions of the glass sphere and read-out electronics. With the chosen parameters a muon rate of about 3 per day is estimated and the maximum measurable angle is around 55°. Measurements of the reflectivity and the transmission spectra of different samples of teflon and reflective foil were discussed and have influenced the design of the housing.

Characterisation measurements of the SiPM arrays have delivered a multiplication factor that helps to compare the different pulse signals. As STRAW-b will be deployed in a cold environment (~ 2°C), the effects of decreasing temperature on the SiPM response have been analysed. Finally, results of first muon measurements in the laboratory have been presented.

Over the next few weeks, the muon tracker and the other modules will be finalised and tested again. The deployment of STRAW-b in the Cascadia Basin is planned for 2020. Together with STRAW, the optical properties of the North Pacific will be further investigated for the development of P-ONE.

Bibliography

[1] M. Boehmer et al. "STRAW (STRings for Absorption length in Water): Pathfinder for a neutrino telescope in the deep Pacific Ocean". In: (2019). arXiv: `arXiv:1810.13265v5`.

[2] E. V. Bugaev et al. "Atmospheric muon flux at sea level, underground, and underwater". In: (1998). ISSN: 15502368. arXiv: `9803488v3 [hep-ph]`.

[3] W. Demtröder. *Experimentalphysik 4 Kern-, Teilchen- und Astrophysik*. 2014. ISBN: 9783642254659.

[4] W. Demtröder. *Experimentalphysik 3 Atome, Moleküle und Festkörper*. 2016. ISBN: 9783662464144.

[5] First Sensor. *Introduction to silicon photomultipliers (SiPMs)*. (Visited on 06/29/2019).

[6] T. Gaisser, R. Engel, and E. Resconi. *Cosmic Rays and Particle Physics*. 2016. ISBN: 9781139192194.

[7] D. Griffiths. *Introduction to elementary particles*. Wiley, 2004. ISBN: 9780471603863.

[8] C. Grupen. *Einstieg in die Astroteilchenphysik*. 2018. ISBN: 9783662552704.

[9] Hardkernel. *Odroid-C2*. URL: `https://www.hardkernel.com/shop/odroid-c2/` (visited on 06/29/2019).

[10] F. Henningsen. "Optical Characterization of the Deep Pacific Ocean: Development of an Optical Sensor Array for a Future Neutrino Telescope MSc thesis". In: (2018).

[11] KETEK GmbH. *Silicon Photomultiplier*. URL: `https://www.ketek.net/sipm/sipm-products/wb-series/` (visited on 06/25/2019).

[12] KETEK GmbH. *Product Data Sheet SiPM Silicon Photomultiplier PM3315-WB*. 2017. URL: `https://www.ketek.net/wp-content/uploads/2018/12/KETEK-PM3315-WB-B0-Datasheet.pdf` (visited on 06/24/2019).

[13] R. Klanner. "Characterisation of SiPMs". In: (2018). ISSN: 01689002. arXiv: `1809.04346v2`.

[14] KM3NeT Collaboration. "Dependence of atmospheric muon rate on seawater depth measured with the first KM3NeT detection units". In: (2019). arXiv: `1906.02704`.

[15] C. Kurtsiefer et al. "The breakdown flash of Silicon Avalanche Photodiodes - back door for eavesdropper attacks?" In: *Journal of Modern Optics* (2001). ISSN: 0950-0340.

[16] W. Leo. *Techniques for Nuclear and Particle Physics Experiments*. 1994. ISBN: 9783540572800.

[17] B.R. Martin and G. Shaw. *Particle Physics*. 2017.

[18] A Neiser et al. "TRB3: a 264 channel high precision TDC platform and its applications". In: (2013). URL: `http://dx.doi.org/10.1088/1748-0221/8/12/C12043`.

[19] B. Povh et al. *Teilchen und Kerne*. 2014. ISBN: 978-3-642-37821-8.

[20] *Quantum Diaries*. URL: `https://www.quantumdiaries.org/2014/03/14/the-standard-model-a-beautiful-but-flawed-theory/` (visited on 06/23/2019).

[21] G. Ros et al. "On the design of experiments based on plastic scintillators using Geant4 simulations". In: (2018). arXiv: `1804.08975v2`.

[22] Saint-Gobain. *BC-400 404 408 412 416*. URL: `https://www.crystals.saint-gobain.com/sites/imdf.crystals.com/files/documents/bc400-404-408-412-416-data-sheet.pdf` (visited on 06/24/2019).

[23] Saint-Gobain. *Scintillation Detectors integrated with SiPM*. URL: `https://www.crystals.saint-gobain.com/products/scintillation-sipm-detector-integration` (visited on 06/24/2019).

[24] Saint-Gobain. *Organic Scintillation Materials and assemblies*. 2015. URL: `https://www.crystals.saint-gobain.com/sites/imdf.crystals.com/files/documents/organics-plastic-scintillators.pdf` (visited on 06/28/2019).

[25] M. Spurio. *Particles and Astrophysics - A Multi-Messenger Approach*. 2016. ISBN: 9783319080505.

[26] M. Sweany et al. "Interaction position, time, and energy resolution in organic scintillator bars with dual-ended readout". In: (2019). ISSN: 01689002. arXiv: `1902.07743v1`.

[27] Christian Tamburini et al. "Deep-Sea Bioluminescence Blooms after Dense Water Formation at the Ocean Surface". In: (2013).

[28] M. Tanabashi et al. *Particle Physics Booklet Extracted from the Review of Particle Physics Particle Data Group*. 2018.

[29] S. Tavernier. *Experimental Techniques in Nuclear and Particle Physics*. 2010. ISBN: 9783642008283.

[30] S. Weingarten. *Szintillationsdetektoren mit Silizium-Photomultipliern*. 2015. ISBN: 9783540773405.